Erosion of a Surface Vortex by a Seamount

Steven Herbette, Yves Morel, Michel Arhan

Erosion of a Surface Vortex by a Seamount

STEVEN HERBETTE AND YVES MOREL

EPSHOM/CMO, Brest, France

MICHEL ARHAN

LPO, CNRS/IFREMER/UBO, Plouzane, France

(Manuscript received 1 July 2002, in final form 12 December 2002)

ABSTRACT

Numerical experiments are carried out on the f plane, using a shallow-water isopycnal model, to analyze the behavior of a surface-intensified anticyclonic vortex when it encounters an isolated seamount. The advection by the vortex of deep fluid parcels across the isobaths is known to generate deep anticyclonic and cyclonic circulations above and near the bathymetry, respectively. These circulations are shown to exert a strong shear on the upper layers, which causes an erosion of the initial vortex by filamentation. The erosion often results in a subdivision of the eddy. While the eroded original structure forms a dipole with the deep cyclone and is advected away, the filaments torn off from the original core aggregate into a new eddy above the seamount. Splitting in more than two structures is sometimes observed. The erosion process is quantified by the bulk volume integral of the eddy potential vorticity anomaly. A sensitivity study to different parameters of the configuration (distance between vortex and seamount, vortex radius, seamount radius, seamount height, or stratification) shows that the intensities of the deep anticyclonic and cyclonic circulations and the vortex erosion are governed both by the reservoir of positive potential vorticity associated with the seamount and by the strength of the cross-isobath flow induced by the eddy.

1. Introduction

This study was initially motivated by observations of Agulhas ring subdivisions caused by seamounts, shortly after their formation. Agulhas rings are surface-intensified large anticyclonic vortices that are spawned from the Agulhas current retroflection and then propagate northwestward in the South Atlantic. Because they are associated with high sea surface height perturbations, one can take advantage of the data provided by satellite altimetry to locate and track them (e.g., Gordon and Haxby 1990). Using this technique, Arhan et al. (1999) back-tracked some rings that they had previously studied at sea. They then suggested that two of them resulted from a single structure that had split when passing over isolated seamounts, at the exit of the Agulhas retroflection region. Schouten et al. (2000), by also analyzing altimetric data, showed evidence that such splitting events were not exceptional and confirmed that subdivision was linked to the eddy propagation over isolated seamounts. Those authors pointed out that of 21 rings formed between 1993 and 1996, 6 were subdivided at least once. Therefore, the subdivision process, which influences the paths of the structures and their rates of dissipation, is of significant importance, at least for Agulhas rings and likely for other vortex species.

So far, many studies have focused on the displacement of oceanographic vortices over a bottom slope. There actually exist analogies between the planetary β effect and the effect of constant bottom slopes (named topographic β effect): both effects are similar for barotropic flows. When stratification is taken into account, some differences exist, but the influence of both processes on the dynamics of vortices relies on their associated potential vorticity (hereinafter referred to as PV) gradient (McWilliams and Flierl 1979; Nof 1983; Smith and O'Brien 1983; Mory 1985; Sutyrin and Flierl 1994; Sutyrin and Morel 1997; Morel and McWilliams 1997). This PV gradient generally induces a westward[1] displacement for all vortices, with an additional northward or southward component for cyclonic or anticyclonic vortices, respectively.

For dissipation, because an oceanic vortex can be scattered by Rossby waves on the planetary β plane (McWilliams and Flierl 1979), a similar effect is expected for the topographic β. Kamenkovich et al. (1996), LaCasce (1998), and Thierry and Morel (1999)

Corresponding author address: Steven Herbette, EPSHOM, CMO/RE, 13, rue du Chatellier, B.P. 30316, Brest CEDEX 29603, France. E-mail: herbette@shom.fr

[1] For the topographic β effect, north is toward shallow depths.

showed that a vortex propagating over a steep bottom slope evolves toward a compensated state in which there is no motion in the lower layers. Dispersion also strongly depends on the vortex size: for large vortices, topographic waves have a strong signature in the surface layers also and contribute to the dispersion of the whole structure, even in the upper layers (Thierry and Morel 1999).

The encounter of an eddy with an isolated topographic obstacle is different and more complicated than with a constant slope. Carnevale et al. (1991) have carried out numerical and tank experiments for small barotropic vortices. They show that, when approaching an isolated seamount, the path of small vortices is downhill for anticyclones whereas cyclones climb up the seamount with trajectories describing spirals. For larger vortices, their experiments led them to the conclusion that the trajectories are then very sensitive to the initial conditions, because of the formation of topographic vortices. In fact, Huppert (1975), Huppert and Bryan (1976), Verron and Le Provost (1985), and Smith (1992) showed how a large-scale current over an isolated seamount can lead to the formation of a cyclone downstream and an anticyclone upstream of the seamount. In the experiments of Carnevale et al. (1991), these newly formed eddies are generated by the original vortex and can in turn interact with the latter. However, Carnevale et al. (1991) have not explored the consequences of such interactions. Van Geffen and Davies (2000) have more recently considered larger barotropic vortices on the β plane. They clearly show that the formation of topographic eddies can strongly affect the original vortex path. An approaching anticyclone can either be deflected from its planetary β trajectory or form a coherent dipole with the cyclonic eddy. This modon (cyclone–anticyclone vortex pair) is found to be able to self-propagate away from the topography in a direction opposite to the initial incoming path of the vortex. Nevertheless, neither of those studies mentioned a splitting event or gave information about the dissipation associated with eddy–seamount encounters. This aspect has been studied in the case of collision of a vortex with an island (Wang and Dewar 2003; Simmons and Nof 2000; Cenedese 2002; Dewar 2002). In this case, as the incoming vortex hits the sidewall of the obstacle, part of the eddy mass situated on the edge forms a jet along the island, which erodes the vortex. When the jet emerges on the other side of the seamount, it leads to the formation of a new eddy. Dewar (2002) recently showed that an isolated seamount could have drastic consequences on the dynamics of a vortex constituted of opposite-sign PV anomalies initially vertically aligned. As in Morel and McWilliams (1997), a hetonic structure usually emerges and modifies the propagation of the structure, but it is also shown that the lower-layer PV pole can be trapped by the seamount and can separate from the upper-layer vortex. The erosion of the latter has, however, not been studied.

In this paper, we extend the Carnevale et al. (1991) and Van Geffen and Davies (2000) studies to a stratified ocean. We focus on the erosion of a surface-intensified anticyclonic vortex as it encounters a seamount, and, in particular, we analyze the processes leading to filamentation and splitting of the anticyclone. We limit the experiments to the f plane, after observing from a few trials that this was a useful first step toward the understanding of the more complex β-plane flows. The f-plane simplification also makes it easier to analyze the influence of several eddy or seamount parameters on the erosion process. In section 2, we describe the numerical model and present the setup of the numerical experiments. Section 3 is dedicated to a basic experiment in which we show that a vortex can split as it encounters a seamount, and we discuss the mechanisms leading to this splitting event. The sensitivity of the eddy erosion to several parameters (distance between vortex and seamount, vortex radius, seamount radius, seamount height, and stratification) is studied in section 4, before a brief conclusion.

2. Model and initial configuration

a. Equations and numerical model

We consider the primitive equations written in isopycnal coordinates (Bleck and Boudra 1986; Bleck and Smith 1990; Bleck et al. 1992), which, when discretized vertically, boil down to the well-known shallow-water equations. In this study, we consider an ocean constituted of three layers, and the equations are then for each layer $k = 1$ to 3:

$$\partial_t u_k + (\mathbf{u}_k \cdot \boldsymbol{\nabla})u_k - fv_k = -\partial_x \mathcal{M}_k + F_x,$$

$$\partial_t v_k + (\mathbf{u}_k \cdot \boldsymbol{\nabla})v_k + fu_k = -\partial_y \mathcal{M}_k + F_y, \quad \text{and}$$

$$\partial_t h_k + \operatorname{div}(h_k \mathbf{u}_k) = 0. \tag{1}$$

Here $\mathbf{u} = (u, v)$ is the horizontal velocity field, f is the constant Coriolis frequency, h is the thickness of an isopycnal layer, and $\mathcal{M}$ is the Montgomery potential (pressure along an isopycnal surface), which can be related to h:

$$\mathcal{M}_k = \sum_{i=1}^{i=3} gh_i + \sum_{i=1}^{i=k-1} \frac{\rho_i - \rho_k}{\rho_o} gh_i, \tag{2}$$

where ρ_k is the density of layer k, ρ_o is a reference density, and g is the earth gravity. Last, $\mathbf{F} = (F_x, F_y)$ represents isopycnal diffusion of momentum and is generally associated with a harmonic or biharmonic operator. When the latter is neglected, PV is conserved for each particle of the flow (see Ertel 1942; Pedlosky 1987). For each layer (bounded by isopycnal surfaces), PV is written

$$\mathrm{PV} = \frac{\zeta + f}{h},$$

where $\zeta = \partial_x v - \partial_y u$ is the relative vorticity. It is also

convenient to define another quantity that we will refer to as PV anomaly (PVA):

$$\mathrm{PVA} = H\left(\frac{\zeta + f}{h} - \frac{f}{H}\right) = \frac{H}{h}\left[\zeta - \frac{f(h - H)}{H}\right], \quad (3)$$

where H is constant and represents the layer thickness at rest. Because PVA is a linear function of PV it has the same conservation properties. In the following, PVA will thus be used as a tracer, in particular to evaluate the erosion of the vortex core. Also notice that in the present configuration PVA filters out the value of the PV at rest and is thus a good indicator of the strength of the (geostrophic) circulation (or vortex strength here). Last, in the limit of small layer-depth variations, PVA reduces to $\zeta - f(h - H)/H$, which is the well-known expression of PV in the quasigeostrophic framework, with ζ representing the relative vorticity and $-f(h - H)/H$ the stretching effect.

Equations (1) are solved numerically using the Miami Isopycnal Coordinate Ocean Model (MICOM: Bleck and Boudra 1986; Bleck and Smith 1990; Bleck et al. 1992). MICOM has, however, been modified to include a fourth-order scheme for the nonlinear advective terms in the momentum equations and a biharmonic diffusion operator for $\mathbf{F}$ (Morel 2001):

$$F_x = \partial_x(\nu\partial_{x^3}u) + \partial_y(\nu\partial_{y^3}u) \quad \text{and}$$

$$F_y = \partial_x(\nu\partial_{x^3}v) + \partial_y(\nu\partial_{y^3}v), \quad (4)$$

Here ν depends on the local velocity modulus and the deformation rate:

$$\nu = \max(C_s^1\Delta x^3|\mathbf{u}|, C_s^2\Delta x^2\sigma), \quad (5)$$

where Δx represents the grid step, $\sigma = [(\partial_x u - \partial_y v)^2 + (\partial_x v + \partial_y u)^2]^{1/2}$ is the deformation tensor, and $C_s^{1,2}$ are nondimensional coefficients. Discretization is associated with truncation errors that depend on the chosen scheme. For the fourth-order scheme used here, the leading-order correction is a dispersive term (velocity multiplied by the fifth derivative of the velocity), and a coefficient $C_s^1 = 1/32$ has been chosen so as to overcome its effects for all wavenumbers that the grid can handle. Here C_s^2 is more subtle to choose because its purpose is to overcome the formation of noise when discontinuities of the velocity field (shocks) develop (e.g., when frontal configurations are studied or when a layer disappears). Experiments with dam-breaking configurations showed that a value $C_s^2 = 1$ was sometimes necessary to keep noise from developing. However, in this study, such values were not necessary, and a coefficient $C_s^2 = 0.05$ was adopted (notice that sensitivity experiments have been carried out with $C_s^2 = 0.05$–0.1 to check that diffusion played a modest role here). Last, the original MICOM schemes rely on a time-splitting technique that separates the fast barotropic modes from the slower baroclinic modes with different Courant–Friedrichs–Lewy (CFL) conditions for each resolution. The time stepping of the baroclinic part uses a second-order leapfrog scheme, and the barotropic mode is based on an Euler scheme that does not conserve second-order accuracy for the slow motion (the barotropic part of the slow motion is also actually calculated with an Euler time-stepping scheme). In the version of the code we have used, the time-stepping scheme was thus also modified so as to be of second order for the slow motions (Y. Morel 2001, personal communication).[2]

b. Initial configuration

For most of the study, we consider a fixed background stratification with layer thicknesses at rest of $H_1 = 300$ m, $H_2 = 500$ m, and $H_3 = 4000$ m and densities $\rho_1 = 1000$ kg m^{-3}, $\rho_2 = 1000.85$ kg m^{-3}, and $\rho_3 = 1001.5$ kg m^{-3}. These thickness values and density differences between layers were chosen with reference to Agulhas ring observations in Arhan et al. (1999). The size of the domain is chosen to be large enough to avoid side effects. Numerical simulations are performed in a closed square domain of 1500×1500 km^2 with a grid step $\Delta x = 10$ km. The size of the domain has been doubled for a few experiments and no qualitative or quantitative differences have been found with the original configuration, which proves that boundaries do not influence the processes studied here. The Coriolis parameter is $f = 7 \times 10^{-5}$ s^{-1}.

The seamount is located near the center of the domain (its exact position is $X = 600$ km, $Y = 750$ km) and has a Gaussian shape (Figs. 1, 2): $h_T(r) = H_T \exp(-r^2/R_T^2)$ with a maximum height H_T and a horizontal length scale R_T (r is the horizontal distance from its center).

We decide to specify our initial vortex as an isolated PVA in the top two layers (Fig. 1). As already mentioned, PVA is a Lagrangian tracer of the shallow-water equations. Another advantage of controlling the PVA of the initial vortex has to do with its stability properties: because we are interested in the splitting of a surface vortex when it encounters a seamount, splitting resulting from intrinsic barotropic or baroclinic instabilities has to be avoided. We thus carefully chose the PVA profile of the initial vortex. To avoid instability, we follow Carton and McWilliams (1989) and chose, in each layer $k = 1$ to 3,

$$\mathrm{PVA}_k = \Delta Q_k^0\left(1 - \frac{r^2}{R_v^2}\right)\exp\left(-\frac{r^2}{R_v^2}\right), \quad (6)$$

where r is the distance from the center of the vortex. Here ΔQ_k^0 is the maximum PVA in layer k and measures the vortex strength, and R_v is the vortex radius, which

[2] Notice that the fact that part of the slow motion—the barotropic component—is solved with a Euler time stepping can also cause some CFL problems, in particular for the diffusion operator.

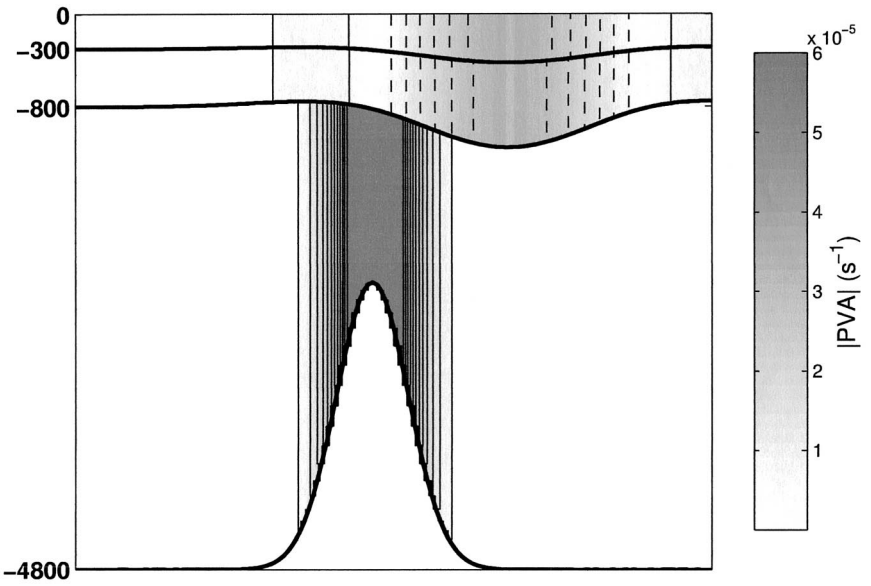

FIG. 1. Cross section of the initial absolute value of PVA in a typical experiment. A seamount with a Gaussian shape is located eastward of a surface anticyclone. Notice the vortex negative PVA (dotted contours) is concentrated in the surface and intermediate layer whereas the bottom-layer parcels of fluid located above the seamount have high positive PVA values (plain contours).

roughly corresponds to the radius of maximum velocity. In the following we chose $\Delta Q_1^0 = \Delta Q_2^0$ and $\Delta Q_3^0 = 0$.

Carton and McWilliams (1989) show that this profile is only slightly unstable in a quasigeostrophic formalism and that the vortex core remains coherent (the positive PVA ring forms two cyclonic poles that do not alter the latter). Notice that, because there is no PVA in the bottom layer and both upper layers have the same PVA structure, baroclinic instability is avoided. This profile has been tested on the f plane in the shallow-water framework for different vortex radii and strengths and has been found to be stable.

By assuming cyclogeostrophic balance, the initial velocity and layer depth fields can be calculated. Details of the PVA inversion method are given in the appendix. The absence of any kind of β effect or weak mean advective background current makes the vortex a stationary solution of the nonviscous primitive equations. In the absence of any topography, the cyclogeostrophic vortex remains steady and stable and does not move. Therefore, to trigger its erosion mechanism induced by an isolated seamount, we must initially place it in the vicinity of the topography. The surface eddy is initially located close to the seamount at a distance d (Fig. 2).

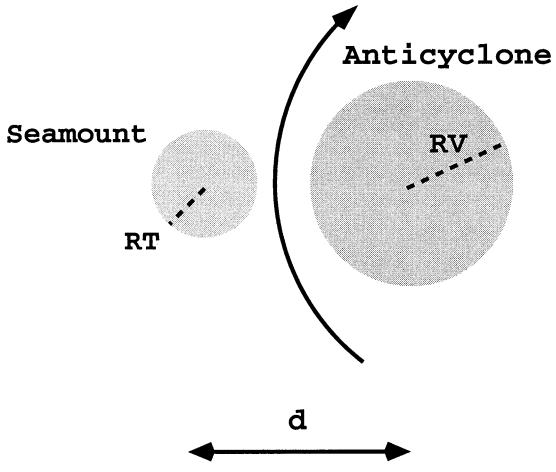

FIG. 2. Top view of the initial setup.

c. Governing parameters

It is convenient to consider the shallow-water Eqs. (1) in nondimensional form using the first internal radius of deformation, $R_d = 33$ km, as length scale (for the chosen stratification) and the inverse of the maximum vortex PVA as timescale, $T = 1/\Delta Q_v^0$. Neglecting the dynamics of gravity waves (Herbette and Morel 2001, unpublished manuscript), Eqs. (1) have five nondimensional parameters: the Rossby number $\epsilon = 1/fT = \Delta Q_v^0/f$ characterizing the ageostrophic effects, the Reynolds number $\mathrm{Re} = \nu/\Delta Q_v^0 R_d^4$ characterizing the effect of viscosity and that will be neglected here, and three Burger numbers $\mathrm{Bu}_1 = g/fR_d$, $\mathrm{Bu}_2 = g(\rho_2 - \rho_1)H_1/\rho_0 fR_d^2$, and $\mathrm{Bu}_3 = g(\rho_3 - \rho_2)H_2/\rho_0 fR_d^2$, characterizing the effect of stratification (the latter are fixed in most of the study). In addition to the five nondimensional parameters, four additional parameters characterize the present configuration: R_v/R_d (the nondimensional vortex radius), d/R_d (the nondimensional initial distance between the vortex and the seamount), R_T/R_d (the non-

dimensional seamount radius), and $fH_T/H_3\Delta Q_v^0$ (the nondimensional seamount height; notice the latter represents the ratio between the maximum PVA associated with the seamount and the vortex).

This number of parameters makes the seamount–vortex encounter a complicated initial-value problem with nine independent nondimensional parameters. It is obvious that it is not possible to study the whole range of parameter values, and our aim is to give an overview of the possible dynamical regimes of eddy–seamount encounters and to focus on physical interpretations of the splitting and filamentation processes. In the following, keeping in mind the behavior of Agulhas rings, we use the dynamical quantities in their dimensional form. The results can, however, be generalized to other vortex types with similar values of the above nondimensional numbers.

3. Reference experiment

a. Parameter choice and results

The parameters that characterize the vortex are first chosen so as to represent approximately the Agulhas rings and the characteristics of the seamount they may encounter: $\Delta Q_1^0 = \Delta Q_2^0 = 0.7f$ ($\Delta Q_3^0 = 0$) and $R_v = 160$ km (notice that $R_v/R_d \simeq 5 \gg 1$). As already mentioned, in the absence of any topography, the cyclogeostrophic vortex remains steady. Numerical viscosity is therefore the only source of erosion and is insignificant for the resolution we have considered ($R_v/\Delta x, y = 16$). We then initially place that vortex in the vicinity of a seamount with characteristics $R_T = 60$ km and $H_T = 2500$ m, at a distance equal to the vortex radius $d = R_v = 160$ km.

Figure 3 shows the PVA evolution in the intermediate layer: the anticyclonic vortex no longer stays axisymmetric and coherent. It is widely elongated and breaks into two main cores with many filaments torn apart. One pole stays trapped over the seamount and takes an axisymmetric form very rapidly. The other core takes an elliptic shape and experiences strong filamentation. It is rapidly advected eastward away from the topography. This simple idealized numerical simulation has therefore been able to reproduce the ability, for a seamount located in the vicinity of a surface anticyclonic eddy, to induce erosion both through filamentation and through splitting of the surface vortex.

b. Interpretation

The evolution of the PVA in the bottom layer is shown in Fig. 4. Notice that, in this layer, the seamount is initially associated with a strong positive PVA of maximum strength $fH_T/H_3 \simeq 0.6f$, comparable with the maximum absolute value of the vortex PVA in the two upper layers. As the anticyclonic circulation, induced by the negative PVA cores in the upper layers, advects fluid parcels over the seamount, it rapidly deforms the bottom PVA field. Part of the initial positive PVA pole detaches from the seamount as visualized in Fig. 4, inducing a cyclonic bottom circulation to the east of the topography. At the same time, some water from above the flat part of the bottom is advected over the seamount, setting up an anticyclonic circulation on top of it. In Fig. 4, this negative relative vorticity above the bathymetry is detected through a diminished PVA signal. Coming back to the intermediate layer (Fig. 3), we see that the deep anticyclone and cyclone, in turn, deform the original vortex, initially into a crescent-shaped feature and then into a long filament-shaped pattern. The westernmost tip of the crescent is constituted of negative PVA advected by the deep anticyclone to the seamount center, where it accumulates. The other tip of the crescent (the northeastern one in panel ''10 days'' of Fig. 3) evolves differently, because it is not trapped above the bathymetry. Its more developed filamentation reflects advection by the deep cyclone. After about 40 days, an eastward advection of the initial vortex itself (or what remains of it) by the cyclone becomes evident. The trajectories of the main surface anticyclone and bottom cyclone are plotted in Fig. 5. They are typical of a baroclinic dipole (also called heton; Hogg and Stommel 1985) self-propagating away from the topography.

The above description of Figs. 3 and 4 shows that the vortex behavior is closely related to the generation of the deep vortices above the submarine obstacle. The formation of such deep eddies over an isolated obstacle, when a large-scale current flows over it, has already been studied for barotropic flow by Huppert (1975) and Verron and Le Provost (1985) and for stratified fluids by Huppert and Bryan (1976). For better evidence of the role of the topographic eddies, we show in Fig. 6 the velocity and PVA fields of the intermediate layer. Notice the strong cyclonic and anticyclonic circulations developing in the initial vortex vicinity. The elliptic shape of the main PVA core is evidently associated with this circulation, as well as the generation of filaments that wrap around the newly formed eddies. As long as filamentation only is involved, both deep circulations play a symmetrical role. However, it is the locking of the deep anticyclone above the seamount that causes the low PVA filaments entrained by this eddy to accumulate at this location, resulting, after about 40 days, in a division of the original vortex into two parts.

Filamentation of a vortex when subject to a background shear has been studied for two-dimensional flows by Legras and Dritschel (1993a,b), Polvani and Flierl (1989), Mariotti and Legras (1994), and Legras et al. (2001). They show that the background shear is responsible for the elliptic shape and can lead to filamentation when it is larger than the vortex vorticity. Arai and Yamagata (1994) have shown that the presence of a stagnation point (hyperbolic point at which the velocity is null) inside the core of the eddy is a necessary

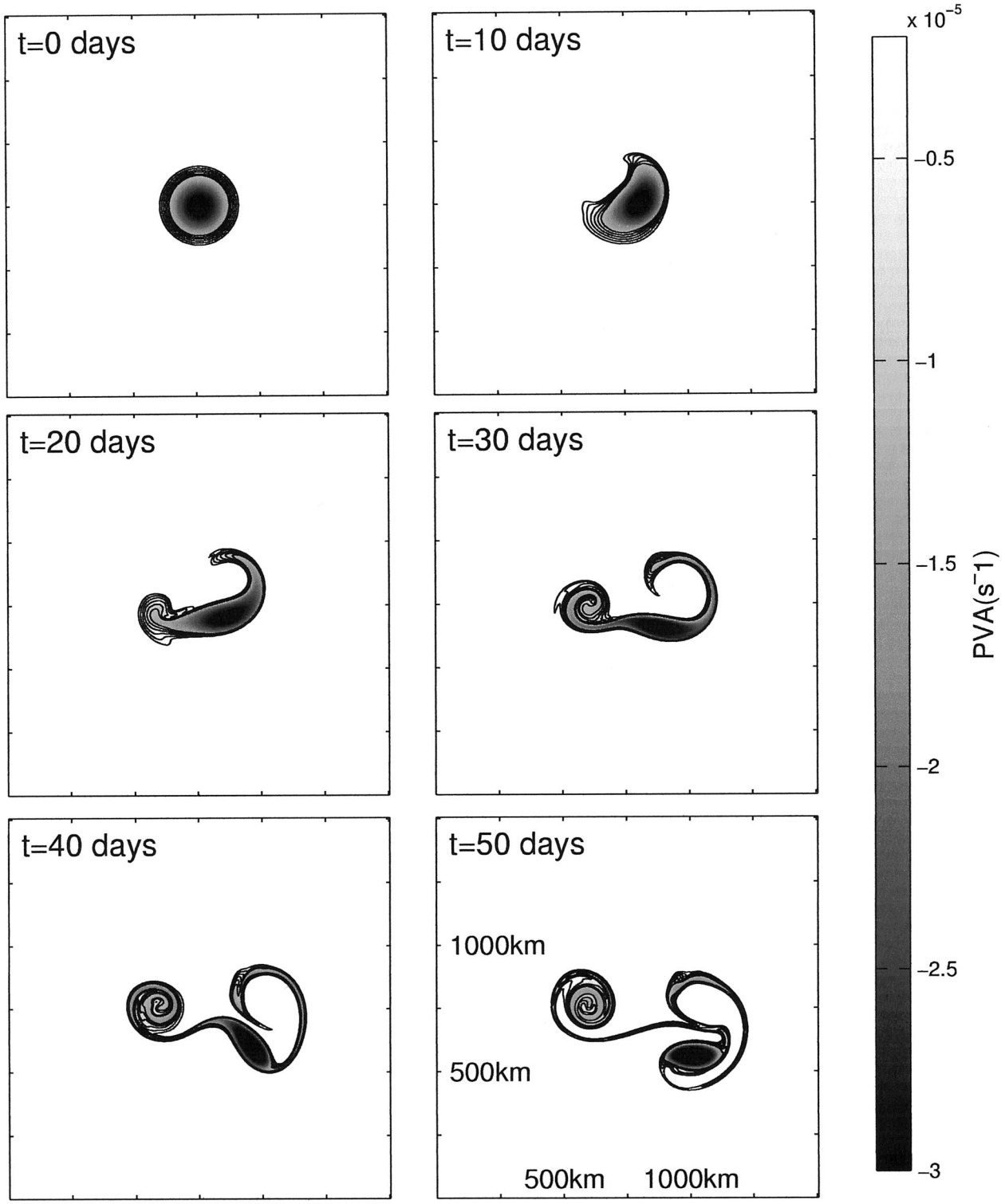

FIG. 3. Evolution of the PVA in the intermediate layer for the reference experiment: $\Delta Q^0_{k=1,2} = -0.7f$, $\Delta Q^0_{k=3} = 0$, $R_\nu = 160$ km, $R_T = 60$ km, $H_T = 2500$ m, and $d = 160$ km. The contour interval is 0.2×10^{-5} s^{-1}.

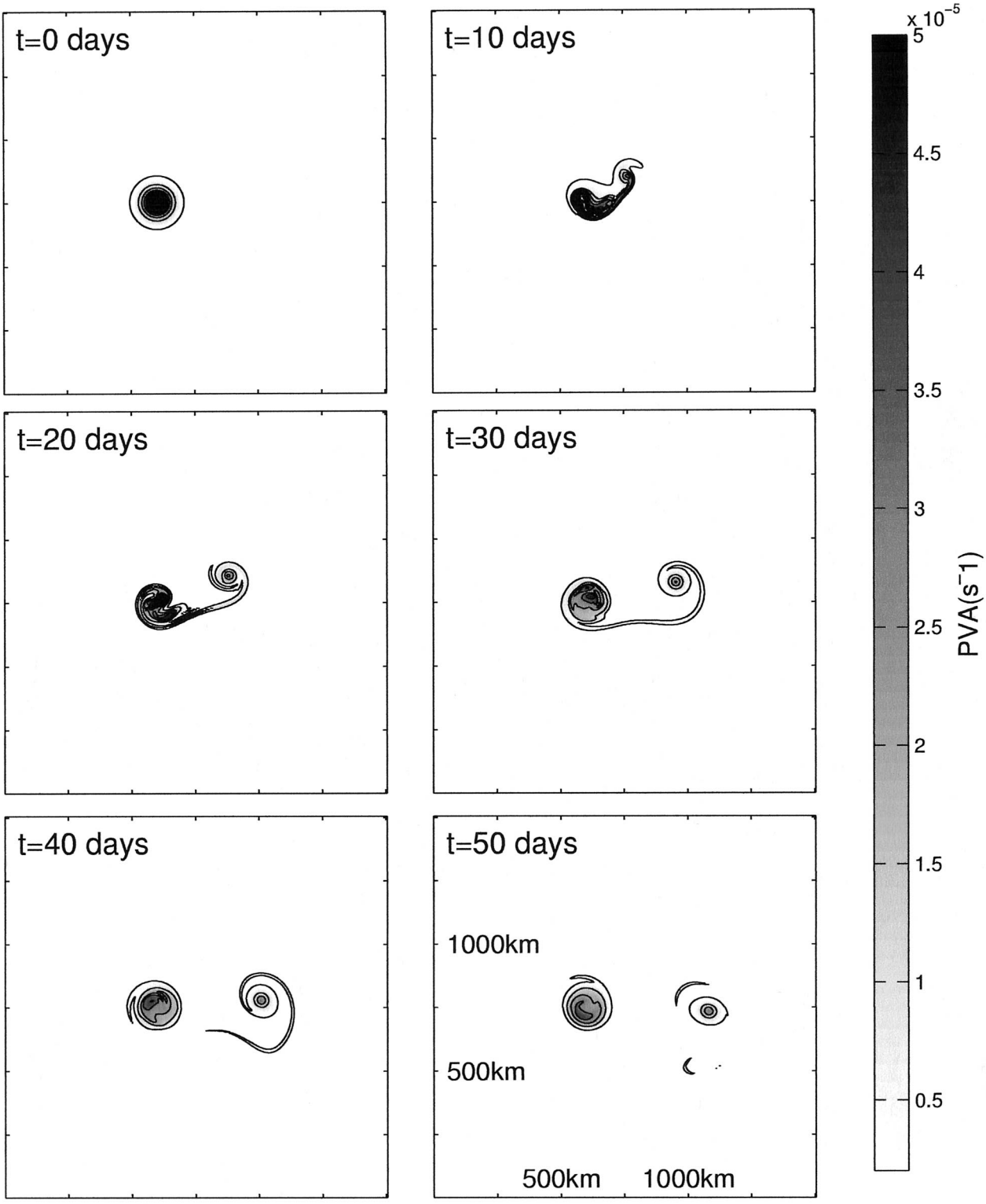

FIG. 4. Evolution of the PVA in the bottom layer for the same experiment as in Fig. 3. The contour interval is now 1.0×10^{-5} s^{-1}.

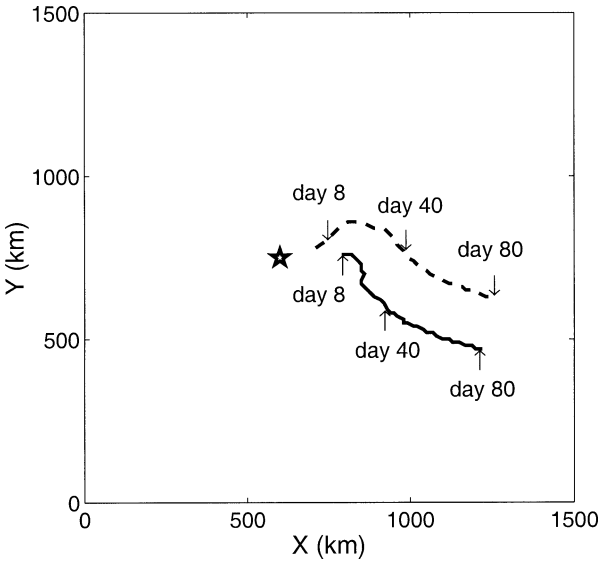

FIG. 5. Trajectory of the bottom topographic cyclone (dashed line) and main surface anticyclonic pole (plain line). The star locates the seamount position.

condition to its subdivision. The Okubo–Weiss quantity (Okubo 1970; Weiss 1991) measures the local influence of the vorticity and shear/strain:

$$\lambda_{ok} = \sigma^2 - \zeta^2. \tag{7}$$

It allows one to distinguish regions that are dominated by vorticity in comparison with regions that are dominated by shear/strain effects. In the latter case, λ_{ok} is positive, the PV field is generally strongly distorted, and filamentation occurs.[3]

In our study, the background shear is associated with the development of the topographic eddies and is particularly strong in the early stage of the encounter, when both the anticyclonic and cyclonic bottom eddies interact with the initial vortex. Figure 6 shows that stagnation points do exist in our simulation between days 10 and 30 (in particular in the region between the seamount-trapped anticyclone and the main core) and are associated with the development of the topographic eddies. Figure 7 represents the Okubo–Weiss quantity at time $t = 20$ days, with the position of one particular stagnation point marked with a star symbol. The latter and Okubo–Weiss criterion both reveal the same thing: the vortex PV field is likely to be strongly deformed, and filaments are likely to be expelled in the region between the vortex core and the seamount.

All of these results indicate that the observed vortex erosion and splitting are associated with the ability of the background shear (itself linked to the anticyclonic and cyclonic topographic eddies) to peel PV filaments from the vortex core. These filaments then give rise to new PV poles or vortices such as the one that stays trapped above the seamount in this reference experiment. We thus expect the erosion and splitting processes to be strongly sensitive to the strength of the topographic eddies with respect to the original vortex strength. We now study the effect of several parameters and their relative influence.

4. Sensitivity analysis

a. Measurement of the vortex erosion

To measure the vortex erosion, we found it convenient to define the quantity:

$$\mathcal{S}_k(t) = \iint_\Omega h_k(x, y)\mathrm{PVA}_k(x, y)\, dx\, dy, \tag{8}$$

which is the bulk volume integral of the PVA over some region Ω. In this study, the latter is chosen as the region in which PVA_k is smaller than a threshold value ($\mathrm{PVA}^{\mathrm{threshold}} = 0$ here) but is also restricted to a threshold radius around the main PVA pole center (here $R_{\mathrm{threshold}} = 1.25R_v$). Different threshold PVA and radius values have been tested, and we found that our results are little sensitive to the chosen values, provided they are not too small or too large. Because PVA is a tracer, it is usually tightly related to the temperature or salinity anomaly inside the core of vortices. Here $\mathcal{S}(t)$ thus quantifies the tracer content of the vortex core. Because it is related to the relative vorticity and velocity field of the vortex, $\mathcal{S}(t)$ also measures the evolution of the vortex strength.

Our numerical results show that splitting and erosion act rapidly so that the final stage is reached after 50 days or so. To estimate the vortex erosion, we thus follow the most intense PVA pole, calculate $\mathcal{S}$ at time $t = 80$ days, and compare it to the initial value $\mathcal{S}(t = 0)$. The parameter

$$R_{\mathrm{fc}} = \frac{\mathcal{S}(t = 80 \text{ days})}{\mathcal{S}(t = 0 \text{ days})} \times 100 \tag{9}$$

thus measures the final PVA content of the vortex, the missing part being located in the filaments and the newly formed PVA pole(s).

b. Distance between the vortex and the topography

Assuming a vortex and a seamount with the same characteristics as in the reference experiment ($\Delta Q^0_{k=1,2} = -0.7f$, $R_v = 160$ km, $H_T = 2500$ m, and $R_T = 60$ km), we vary the initial distance d between the vortex and the topography from 0 to approximately 2 times the vortex radius. Figure 8 represents the dependence of R_{fc}

[3] Notice that this criterion assumes that the tensor $(\nabla_{\mathbf{u}})$ is stationary and that the horizontal divergence is small when compared with the square root of λ_{ok}. Lapeyre et al. (1999) have recently derived, in the framework of two-dimensional flows, a more accurate criterion that takes into account some Lagrangian variations of the tensor $(\nabla_{\mathbf{u}})$. Its accurate calculation, however, requires the gravity waves to be filtered out.

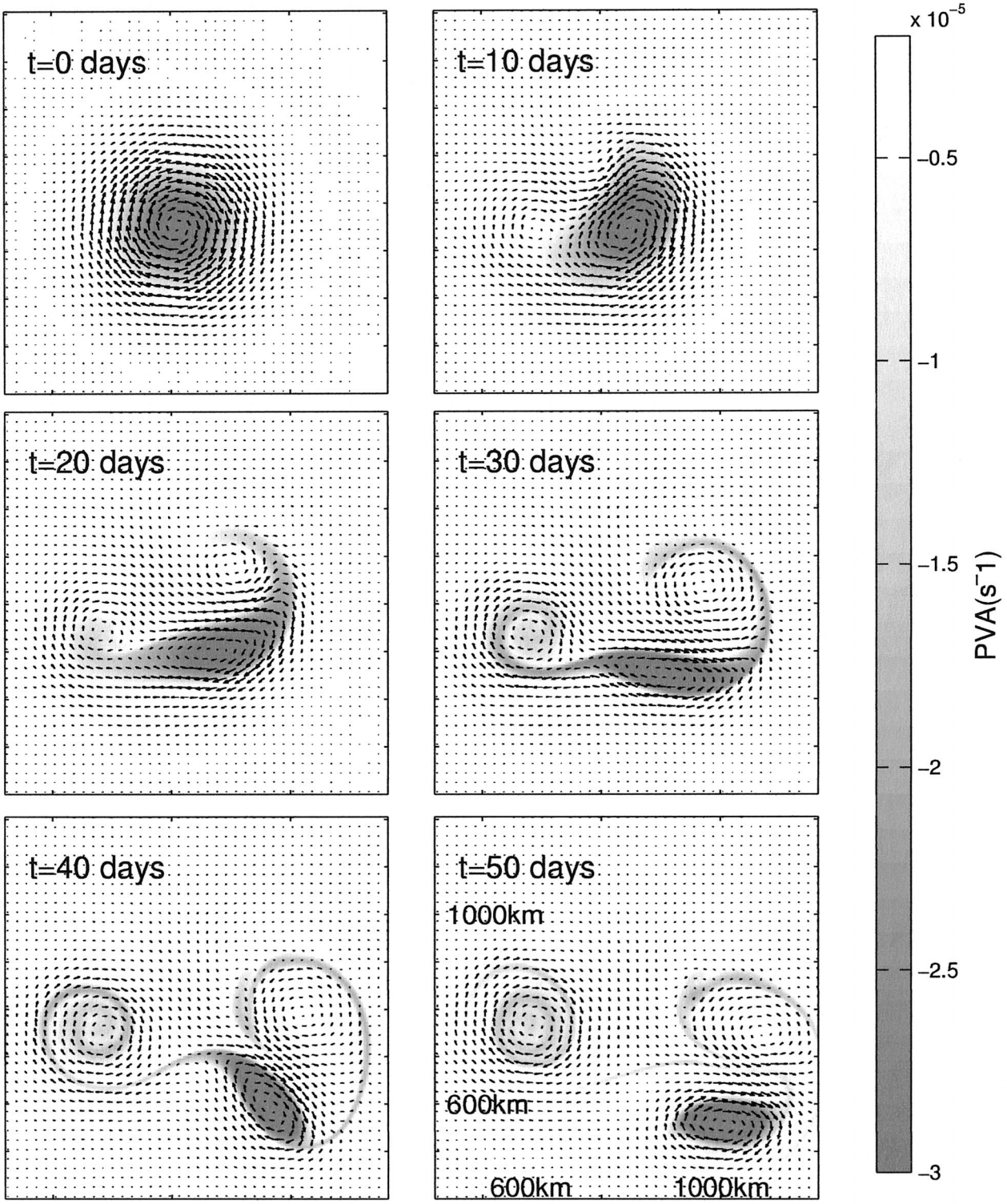

FIG. 6. Same as Fig. 3 except the velocity field is superimposed and we have zoomed in on the area near the vortex.

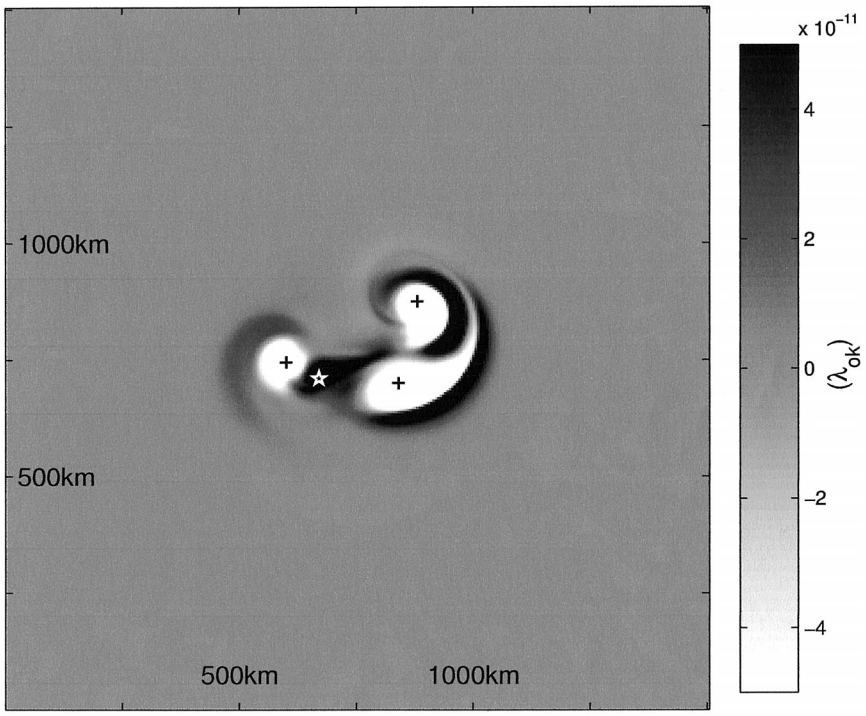

FIG. 7. Okubo–Weiss quantity at time $t = 20$ days in the intermediate layer for the reference experiment. Plus marks are stagnation points in regions where λ_{ok} is negative; the star is a stagnation point in a region where λ_{ok} is positive and therefore represents a filamentation region.

on the initial vortex–seamount distance for both the upper and second layer. Erosion is very efficient when the distance between the vortex and the seamount is close to the vortex radius ($d \simeq R_v$), otherwise it remains weak. In fact, we have seen that the strength of the topographic eddies is related to the strength of the vortex-induced cross-isobath flow above the seamount. When d is small, the circulation associated with the vortex approximately follows the isobaths and no or few fluid parcels are detached from above the seamount. As a result, the topographic eddies are weak and do not have much effect on the upper-layer anticyclone. We have verified that no cyclone is formed and that the surface vortex stays trapped above the seamount. When d increases, the cross-isobath flow also increases and is maximum when the vortex edge is just above the seamount, that is to say, when $d \simeq R_v$. Strong cyclonic and anticyclonic topographic eddies are then generated, which erode the initial vortex as seen in the reference experiment. When d is further increased, the cross-isobath flow associated with the original vortex rapidly diminishes again as the velocity field decreases exponentially beyond the vortex radius. A cyclone detaches from the seamount, but it is too weak to deform the original vortex and generate filamentation. However, it still interacts with the latter, forming a baroclinic dipole that is advected away from the topography. The topographic anticyclone trapped above the seamount is too far from the vortex to interact with it. As seen in the reference experiment, the vortex splits into two main negative PVA poles when erosion is maximum. One stays trapped above the seamount while the other, forming a baroclinic dipole with the bottom cyclone, is advected away. For values of d slightly below R_v, the main PVA pole (with the largest R_{fc})

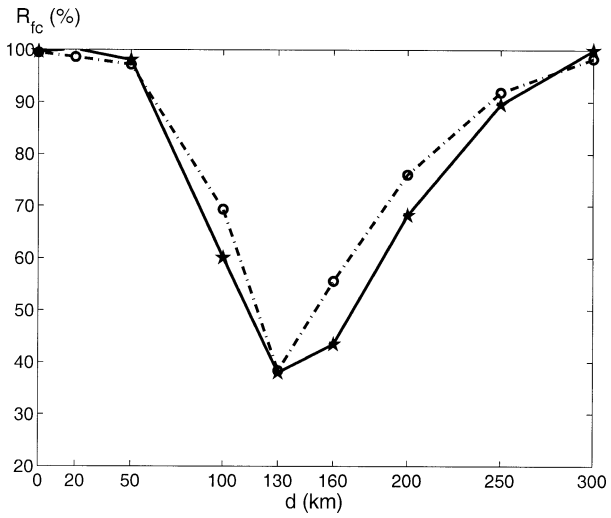

FIG. 8. Anticyclone final PVA content ratio R_{fc} as a function of d for the reference experiment. The surface layer is associated with the dash–dotted line with circles, and the intermediate layer is associated with the plain line with stars.

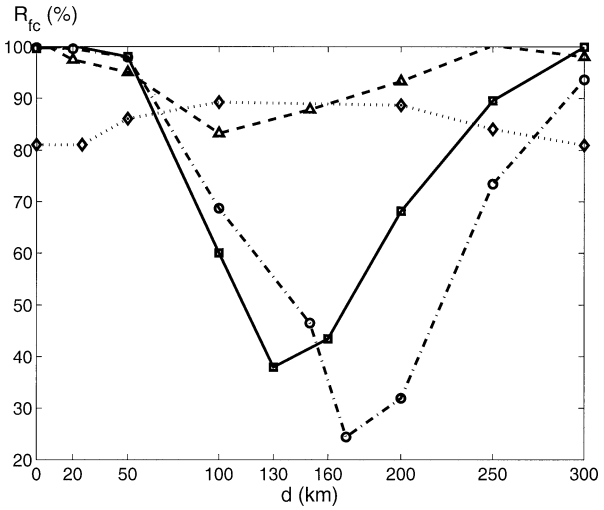

FIG. 9. Sensitivity of the intermediate-layer anticyclone final PVA content ratio R_{fc_2} to the vortex radius. The solid line with squares corresponds to the reference experiment and is the same as in Fig. 8. The dotted line with diamonds corresponds to $R_v = 50$ km, the dashed line with triangles corresponds to $R_v = 100$ km, and the dashed–dotted line with circles corresponds to $R_v = 200$ km.

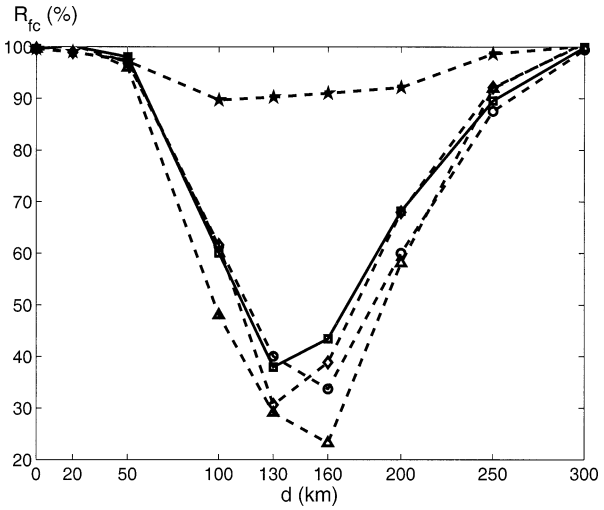

FIG. 10. Sensitivity of the intermediate-layer anticyclone final PVA content ratio R_{fc_2} to the seamount height. The characteristics of the experiments are the same as in the reference configuration except for the seamount height (circles: $H_T = 3300$ m, squares: $H_T = 2500$ m, triangles: $H_T = 1500$ m, diamonds: $H_T = 1000$ m, and stars: $H_T = 500$ m).

is the one above the seamount, and for values of d slightly above R_v, it is the one in the baroclinic dipole.

c. Vortex radius

We now study how varying the surface vortex radius may affect its erosion as it encounters a seamount. Considering intense vortices ($\Delta Q_1^0 = \Delta Q_2^0 = -0.7f$) located in the vicinity of our basic seamount ($R_T = 60$ km and $H_T = 2500$ m), we show in Fig. 9 the final PVA content ratio R_{fc} of the intermediate layer for eddy radii R_v of 50, 100, 160, and 200 km. For each vortex radius, d is varied from 0 to approximately 2 times the vortex radius. Notice the maximum erosion always happens when $d \simeq R_v$.

Figure 9 shows that small surface vortices only weakly dissipate and appear not to feel the seamount, at least when the latter has the characteristics we have chosen. Two effects contribute to decrease the strength of the cross-isobath flow associated with small vortices. First the maximum velocity strongly depends on the ''reservoir'' of negative PVA associated with the initial eddy and thus diminishes with R_v. Second, the influence of a PVA pole on adjacent layers also depends on the vortex radius (it is measured by the Burger numbers) and decreases with R_v also. Except for numerical viscosity effects that cut down the PVA content by about 15%, there is almost no erosion for $R_v = 50$ km, and therefore no filamentation or splitting. For larger radii, the vortex erosion is effective and may lead to a final main PVA pole that contains only about 30% of its initial PVA. The rest has been expelled into filaments and new PVA poles.

d. Seamount height

In the following experiments, we keep the reference values for the vortex structure ($\Delta Q_{k=1,2}^0 = -0.7f$, $\Delta Q_{k=3}^0 = 0$, and $R_v = 160$ km) and vary the seamount height. For each value of H_T, we test the influence of the eddy–seamount initial distance d from 0 to approximately 2 times the eddy radius. The results (Fig. 10) show R_{fc} in the intermediate layer, after 80 days, for H_T values of 500, 1000, 1500, 2500, and 3300 m. Whatever is the seamount height, maximum erosion coincides with an eddy–seamount distance roughly equal to the vortex radius ($d \simeq R_v$), that is to say, when the induced cross-isobath flow in the bottom layer is also maximum. Nevertheless, when $d \simeq R_v$, erosion is low for $H_T = 500$ m and is significantly larger for the other tested heights. This result is expected because the strength of the emerging cyclone is linked to the reservoir of positive PVA associated with the seamount, which obviously increases with the seamount height. Yet, it is surprising to see that erosion is maximum for $H_T \simeq 1500$ m and decreases for higher seamounts. Analysis of the PVA evolution (not shown) reveals that in all experiments with $d \simeq R_v$ a cyclone detaches from the topography. It leads to only slight filamentation for $H_T = 500$ m and to stronger filamentation and splitting for larger values, particularly for $H_T \simeq 1500$ m. In fact, increasing the seamount height also steepens the bottom slope. A strong topographic slope is also associated with a strong topographic β effect, which makes it more difficult for fluid parcels to move across isobaths. This effect counteracts the PVA reservoir increase because it can keep the cyclonic eddy from detaching and limits the strengths of the topographic eddies. Figure 11 shows

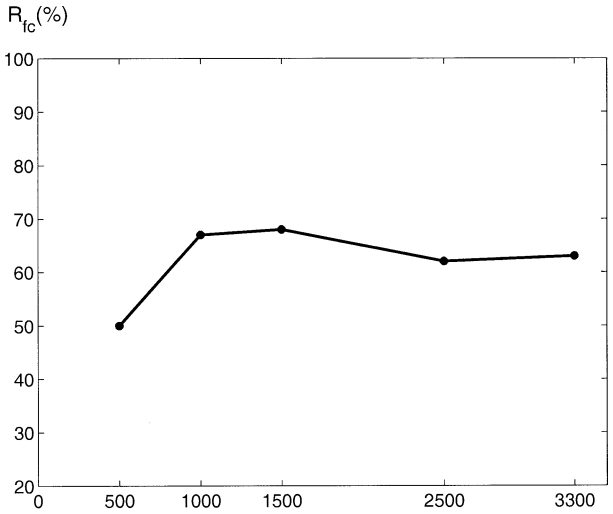

FIG. 11. Strength of the bottom cyclone as a function of the seamount height (here $d = 160$ km is fixed). Note that the maximum is obtained for an intermediate seamount height.

the nondimensional value of the content of the positive PVA pole that leaves the topography in the bottom layer when $d = 160$ km. It is calculated with Eq. 8 and is then scaled by the initial anticyclonic vortex PVA content. We note that the number of positive PVA particles leaving the topography is indeed maximum for $H_T \simeq 1500$ m and slightly decreases for larger values. Notice finally that, in the region between the bottom anticyclone and cyclone, both eddies accumulate their effects on the surface intensified eddy. Besides, because the topographic anticyclone roughly has the same strength as the cyclone,[4] the cumulative effect of the topographic eddies can be evaluated by multiplying the cyclone PVA content by 2. Figure 11 then also shows that, to achieve strong filamentation and splitting, the cumulated PVA content associated with the topographic eddies must be higher than that of the original vortex. This condition is necessary for the circulation associated with the former vortices to be strong enough to create a stagnation point.

e. Seamount radius

The next parameter we have chosen to study is the seamount radius R_T. Like H_T, variations of this parameter modify both the seamount PVA reservoir and the seamount steepness. We thus resume the reference experiment with several values of R_T: 30, 60, 90, and 120 km. The simulation with $R_T = 30$ km is conducted with a thinner grid ($\Delta x, y = 5$ km). All four experiments end up in breaking of the original surface eddy. Nevertheless, as expected, the final erosion is different for each configuration: it is weak for the smaller seamount ($R_{fc} \simeq 80\%$) and increases with larger R_T. Indeed, in this case, there are no counteracting effects: increasing R_T increases the topographic PVA reservoir and diminishes the topographic β effect. It is interesting to notice that, whereas in the reference experiment the original vortex splits into two negative PVA poles, five are created for $R_T = 90$ km including the one trapped on the seamount (Fig. 12), and four poles are created for $R_T = 120$ km. The merging of some of the poles makes it difficult to define a rule for the number of poles created, which eventually depends on the ability of the cyclone to stretch the original vortex, but the possibility to create more than two eddies is illustrated.

f. Stratification

In going back to Fig. 8, we notice that the erosion and splitting processes lead to a vortex with a modified vertical structure, because the negative PVA pole is more eroded in the intermediate layer than in the upper layer: for $d = R_v$, the final PVA content of the surface and second layer vortex, respectively, represents about 40% and 50% of the initial value. In fact, the influence of the topographic eddies decreases upward, because the latter are associated with PVA in the bottom layer only. Therefore, the shear induced by these eddies is larger and filamentation is more effective in the intermediate layer than in the surface layer. This effect is expected to be sensitive to the stratification. We thus resume the reference experiment, keeping the same densities for the upper and intermediate layer and modifying ρ_3. Two different values are studied, one with a smaller density $\rho_3 = 1001.1$ kg m^{-3} and one with a higher density $\rho_3 = 1001.6$ kg m^{-3} ($\rho_3 = 1001.5$ kg m^{-3} in the reference experiment). The corresponding deformation radii are 26 and 36 km, respectively (and 33 km for the reference experiment). Figure 13 shows the final PVA content R_{fc} for each experiment and for each layer in comparison with the reference simulation. The plain-line curves correspond to the reference experiment, the dashed-line curves correspond to $\rho_3 = 1001.6$ kg m^{-3}, and the dash–dotted-line curves correspond to $\rho_3 = 1001.1$ kg m^{-3}. Circles are associated with the surface layer, and stars are associated with the intermediate layer.

We first note that the shapes of the erosion curves remain similar to those of the reference experiment: the erosion is maximum for $d \simeq R_v$ and, in this case, splitting occurs. However, as expected, erosion is stronger when $\Delta\rho_{2-3}$ is weaker. When the stratification between the bottom and intermediate layers $\Delta\rho_{2-3}$ is increased, the circulation, induced in the upper layers by the topographic eddies, decreases. The result of the eddy–seamount encounter therefore becomes less erosive. On the contrary, when $\Delta\rho_{2-3}$ is decreased, the upper-layer

[4] The cyclone and anticyclone are formed because fluid parcels are exchanged between two regions with different PVA: the topography, with high PVA values, and the flat bottom region that corresponds to PVA = 0. Except for their sign, exchanged particles thus correspond to the same anomaly when calculated with respect to their new environment.

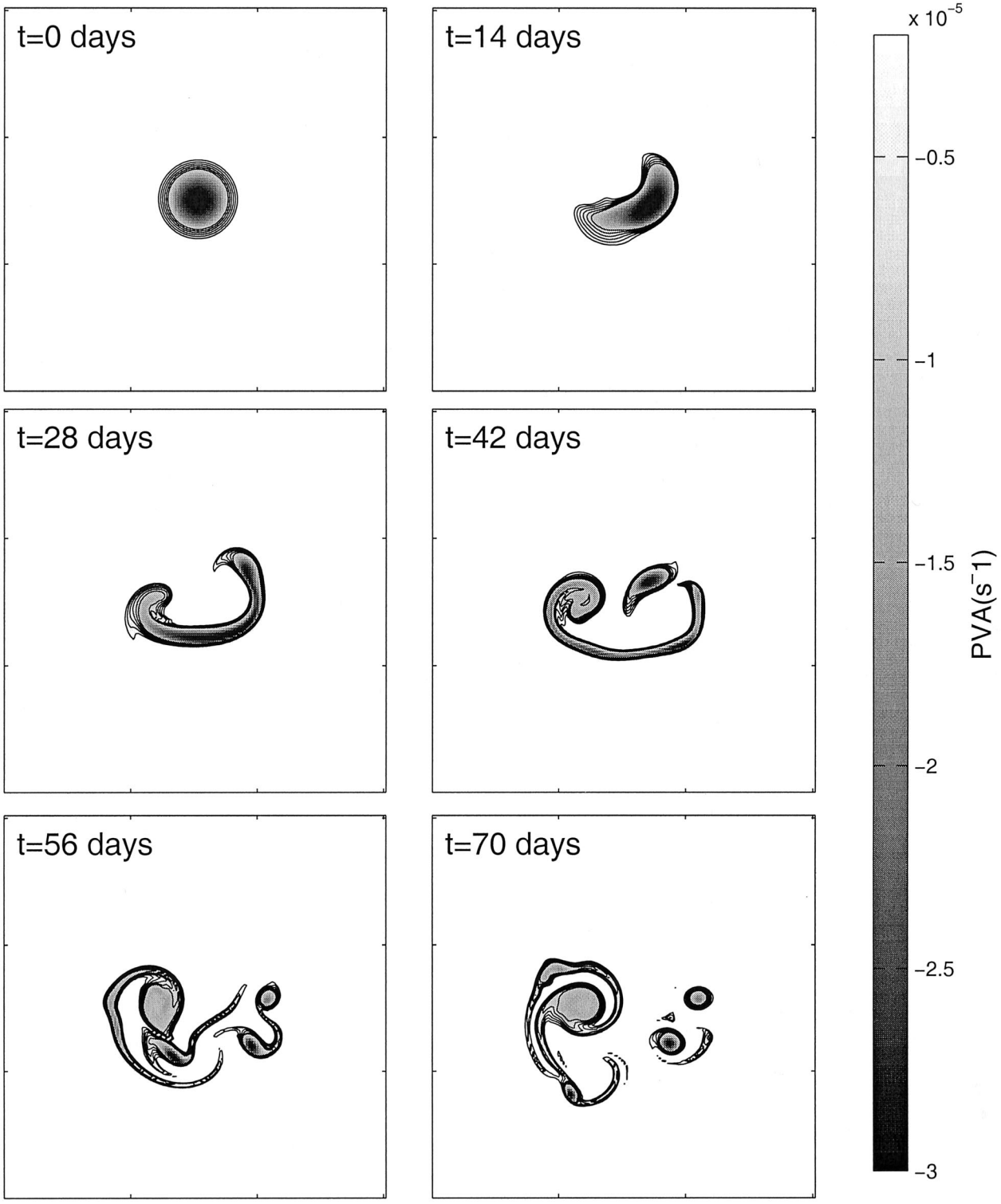

FIG. 12. Evolution of the PVA in the intermediate layer for an experiment with the same characteristics as in the reference experiment except for the seamount radius: R_T = 90 km. Note the many small vortices generated here.

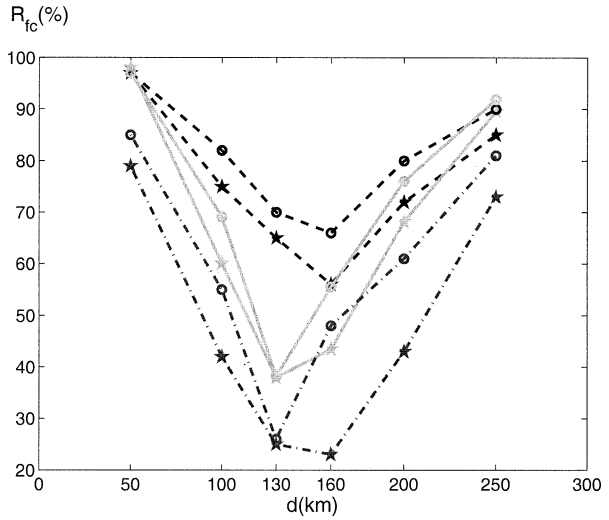

FIG. 13. The surface-layer (circles) and intermediate-layer (stars) anticyclone final PVA content ratios R_{fc} ($k = 1, 2$) are plotted as a function of the eddy–seamount distance for several ambient stratifications. Weak stratification ($\rho_3 = 1001.1$ kg m^{-3}): dashed–dotted lines; reference experiment ($\rho_3 = 1001.5$ kg m^{-3}): plain lines; strong stratification ($\rho_3 = 1001.6$ kg m^{-3}): dashed lines.

signature of the bottom eddies becomes stronger. Thus, more filamentation is expected. In the latter case, the difference between vortex erosion in surface and intermediate layers increases. For a critical eddy–seamount distance $d = R_v$ and a weak stratification ($\rho_3 = 1001.1$ kg m^{-3}), the top surface eddy keeps 49% of its original PVA content after 80 days, whereas the intermediate layer only keeps 22%. Tracers have thus been much more dispersed in the intermediate layer than in the upper layer, and the resulting eddy is more surface intensified than originally.

5. Summary

In this study, we have analyzed the mechanisms intervening at the encounter of a strong anticyclonic surface-intensified vortex with an isolated seamount. The result of this encounter can be very erosive and can lead to the splitting of the original vortex with expelling of PV filaments from the main core. The mechanism is different from the one already proposed by Simmons and Nof (2000) and Cenedese (2002), who addressed the collision of an eddy with an island. In our simulations, erosion stems from the advection of deep water across the isobaths of the topography. The deep cross-isobath flow generates bottom-intensified vortices of either sign, which in turn deform, stir, and often subdivide the initial eddy.

Because the influence of the bottom eddies decreases upward as a function of the ambient stratification, the process is found to be sensitive to the stratification, and the eroded eddy is always more surface intensified than the original one. The sensitivity of the interaction to the vortex and seamount characteristics (vortex radius, seamount radius, and seamount height) is found to be governed by the reservoir of positive PVA associated with the seamount in the bottom layer, by the topography steepness, and by the initial cross-isobath velocity associated with the vortex. Seamounts with small radii or heights have a reduced PVA reservoir, which can limit the strength of the topographic eddies, and the latter will not be able to tear apart strong incoming vortices. In the case of steep seamount slopes, on the other hand, the topographic β effect can keep fluid parcels from being expelled from above the bathymetry. This is another limiting parameter for the generation of topographic eddies sufficiently strong to erode the initial vortex. Another key parameter is naturally the distance between the vortex and the seamount: erosion is maximum when the distance is close to the vortex radius, that is to say, when the cross-isobath flow induced by the vortex is maximum. When the vortex is initially far from the seamount, the deep cyclone generated by the interaction, though weak, may form a baroclinic dipole with the original vortex and advect it away from the topography before significant erosion can occur.

One may then wonder if a vortex propagating toward a seamount can get close enough to the latter so that topographic eddies can first be generated and then induce a critical shear on the approaching eddy. The β-plane experiments carried out by Van Geffen and Davies (2000) have apparently led not to strong erosion but only to deviations of the vortex trajectories. It is clear that more ingredients than considered here would be required for a more realistic approach. For instance, the planetary β effect, or the presence of a mean flow, might help the eddy to move sufficiently close to the seamount to trigger the processes described above. In a similar way, although subdivisions of the initial vortex in more than two structures have been observed, one may wonder which additional process could move away from the seamount the pole that always remains trapped on it. The planetary β effect might also play this part. Moreover, the dynamics of oceanic vortices, in particular of large structures such as Agulhas rings, are generally influenced by the planetary β effect. The presence of β can lead to their substantial erosion and therefore can modify the result of their encounter with topography. Nevertheless, the f-plane experiments that we have carried out constitute a first step toward the understanding of the physical mechanisms that govern an eddy–seamount encounter and will provide a useful insight of the dynamics for more realistic studies.

For the Agulhas rings that we presented as oceanic examples of eddy subdivisions, we may mention the recent increased interest in the cyclonic structures that often are observed to accompany these eddies, particularly in their possible formation processes (Penven et al. 2001). The formation of baroclinic dipoles that we have seen to result from the eddy and seamount en-

counter should also probably be considered in this context.

Acknowledgments. The authors are grateful to Drs. Rainer Bleck, Linda Smith, and Eric Chassignet for the use of MICOM and to Dr. Xavier Carton for stimulating discussions and comments. Support for this study has been provided by the Service Hydrographique et Océanographique de la Marine for Yves Morel and by the Institut Français de Recherche pour l'Exploitation de la Mer for Michel Arhan. Steven Herbette was supported by a grant from the Délégation Générale de l'Armement during his Ph.D thesis.

APPENDIX

Initialization of a Stable Vortex

We consider an N-layer flat-bottom ocean and an axisymmetric vortex in cyclogeostrophic balance. This vortex is associated with a potential vorticity anomaly profile $\Delta Q(r)$. To initialize our shallow-water model, we need to invert the potential vorticity equation and calculate the layer thicknesses and azimuthal velocities associated with the PVA field. In polar coordinates, the system to solve is

$$\frac{\upsilon_{\theta_k}^2}{r} + f\upsilon_{\theta_k} = \partial_r \mathcal{M}_k,$$

$$\mathcal{M}_1 = g\sum_{i=1}^{i=N_c}\Delta h_i,$$

$$\mathcal{M}_k = \sum_{i=1}^{i=k-1}\frac{\rho_i}{\rho_k}g\Delta h_i + \sum_{i=k}^{i=N_c} g\Delta h_i, \quad \text{and}$$

$$\zeta_k - f\frac{\Delta h_k}{H_k} = \Delta Q_k\left(1 + \frac{\Delta h_k}{H_k}\right), \tag{A1}$$

where $\zeta_k = 1/r\partial_r(r\upsilon_{\theta_k})$ is the relative vorticity in polar coordinates, k is the layer subscript, υ_{θ_k} is the azimuthal velocity, $\mathcal{M}_k$ is the Montgomery potential, and $\Delta h_k = h_k - H_k$ is the layer thickness variation. This system of partial derivative equations is not linear because of the quadratic term associated to the centrifugal force υ_θ^2/r and does not admit trivial analytical solutions. We therefore use a numerical iterative method that consists in approaching the quadratic term at each iteration (n) by its value at iteration ($n-1$). The first step of the method ($n = 1$) supposes geostrophic equilibrium, and the quadratic term is simply absent from the equations. To guarantee that our vortex is isolated, we have to ensure that the bulk volume integral of PVA is zero (Morel and McWilliams 1997). To overcome this constraint, we have chosen to fix $F_k = \Delta Q_k(1 + \Delta h_k/H_k)$ instead of ΔQ_k.

The system we invert is the following:

$$(\mathbf{M}\nabla^2\boldsymbol{\Delta h}^n)_k - f^2\frac{\Delta h_k^n}{H_k} = F_k + \frac{1}{r}\partial_r(\upsilon_{\theta_k}^2)^{n-1}, \quad \text{and}$$

$$\upsilon_{\theta_k}^2 = \frac{1}{f}(\mathbf{M}\partial_r\boldsymbol{\Delta h})_k - \frac{(\upsilon_{\theta_k}^2)^{n-1}}{r}, \tag{A2}$$

where $\mathbf{M}$ is the matrix that links the Montgomery potential $\mathcal{M}$ to Δh.

The boundary conditions are

$$\lim_{r\to+\infty}(\partial_r\Delta h_k) = 0, \qquad \lim_{r\to+\infty}\left(\sum_{k=1}^{k=N}\Delta h_k\right) = 0, \quad \text{and}$$

$$\upsilon_\theta(r=0) = 0. \tag{A3}$$

Equations (A2) with the boundary conditions Eqs. (A3) form a linear system of partial derivative equations. The latter is solved by calculating the eigenvalues and eigenvectors of the matrix $\mathbf{M}$. Iterations are stopped when the difference in Δh between two successive iterations is less than a small value ϵ (typically $\epsilon \simeq 1$ mm):

$$\max(|\Delta h^n - \Delta h^{n-1}|) \le \epsilon. \tag{A4}$$

REFERENCES

Arai, M., and T. Yamagata, 1994: Asymmetric evolution of eddies in rotating shallow water. *Chaos,* **4,** 163–175.

Arhan, M., H. Mercier, and J. R. E. Lutjeharms, 1999: The disparate evolution of three Agulhas rings in the South Atlantic Ocean. *J. Geophys. Res.*, **104,** 20 987–21 005.

Bleck, R., and D. Boudra, 1986: Wind-driven spin-up in eddy-resolving ocean models formulated in isopycnic and isobaric coordinates. *J. Geophys. Res.*, **91,** 7611–7621.

——, and L. T. Smith, 1990: A wind-driven isopycnic coordinate model of the north and equatorial Atlantic Ocean. 1. Model development and supporting experiments. *J. Geophys. Res.*, **95,** 3273–3285.

——, C. Rooth, D. Hu, and L. T. Smith, 1992: Salinity-driven thermocline transients in a wind- and thermohaline-forced isopycnic coordinate model of the North Atlantic. *J. Phys. Oceanogr.*, **22,** 1486–1505.

Carnevale, G., R. Kloossterziel, and G. Van Heijst, 1991: Propagation of barotropic vortices over topography in a rotating tank. *J. Fluid Mech.*, **233,** 119–139.

Carton, X., and J. McWilliams, 1989: Barotropic and baroclinic instabilities of axisymmetric vortices in a qg model. *Mesoscale/Synoptic Coherent Structures in Geophysical Turbulence*, Elsevier, 225–244.

Cenedese, C., 2002: Laboratory experiments on mesoscale vortices colliding with a sea-mount. *J. Geophys. Res.*, **107,** 3053, doi: 10.1029/2000JC000599.

Dewar, W. K., 2002: Baroclinic eddy interaction with isolated topography. *J. Phys. Oceanogr.*, **32,** 2789–2805.

Ertel, H., 1942: Ein neuer hydrodynamischer Wirbelsatz (A new scalar to characterize hydrodynamic eddies). *Meteor. Z.*, **59,** 271–281.

Gordon, A. L., and W. F. Haxby, 1990: Agulhas eddies invade the South Atlantic: Evidence from *Geosat* altimeter and shipboard conductivity–temperature–depth survey. *J. Geophys. Res.*, **95,** 3117–3125.

Hogg, N., and H. Stommel, 1985: The heton, an elementary interaction between discrete baroclinic geostrophic vortices, and its implication concerning eddy heat-flow. *Proc. Soc. London,* **370,** 1–20.

Huppert, H., 1975: Some remarks on the initiation of inertial Taylor columns. *J. Fluid Mech.,* **67,** 397–412.

——, and K. Bryan, 1976: Topographically generated eddies. *Deep-Sea Res.,* **23,** 655–679.

Kamenkovich, V. M., Y. P. Leonov, D. A. Nechaev, D. A. Byrne, and A. L. Gordon, 1996: On the influence of bottom topography on the Agulhas eddy. *J. Phys. Oceanogr.,* **26,** 138–140.

LaCasce, J. H., 1998: A geostrophic vortex over a slope. *J. Phys. Oceanogr.,* **28,** 2362–2381.

Lapeyre, G., P. Klein, and B. Hua, 1999: Does the tracer gradient vector align with the strain eigen-vectors in 2d turbulence? *Physica D,* **A11,** 3729–3737.

Legras, B., and D. Dritschel, 1993a: A comparison of the contour surgery and pseudo-spectral methods. *J. Comput. Phys.,* **104,** 287–302.

——, and ——, 1993b: Vortex stripping and the generation of high vorticity gradients in two-dimensional flows. *Appl. Sci. Res.,* **51,** 445–455.

——, ——, and P. Caillol, 2001: The erosion of a distributed two-dimensional vortex in a background straining flow. *J. Fluid Mech.,* **441,** 369–398.

Mariotti, A., and B. Legras, 1994: Vortex stripping and the erosion of coherent structures in two-dimensional flows. *Phys. Fluids,* **6,** 3954–3962.

McWilliams, J. C., and G. R. Flierl, 1979: On the evolution of isolated, nonlinear vortices. *J. Phys. Oceanogr.,* **9,** 1155–1181.

Morel Y., and J. McWilliams, 1997: Evolution of isolated interior vortices in the ocean. *J. Phys. Oceanogr.,* **27,** 727–748.

Mory, M., 1985: Integral constraints on bottom and surface isolated eddies. *J. Phys. Oceanogr.,* **15,** 1433–1438.

Nof, D., 1983: The translation of isolated cold eddies on a sloping bottom. *Deep-Sea Res.,* **30,** 171–182.

Okubo, A., 1970: Horizontal dispersion of floatable particles in the vicinity of velocity singularities such as convergences. *Deep-Sea Res.,* **17,** 445–454.

Pedlosky, J., 1987: *Geophysical Fluid Dynamics.* Springer-Verlag, 710 pp.

Penven, P., J. Lutjeharms, P. Marchesiello, C. Roy, and S. Weeks, 2001: Generation of cyclonic eddies by the Agulhas current in the lee of the Agulhas bank. *Geophys. Res. Lett.,* **27,** 1055–1058.

Polvani, L., and G. Flierl, 1989: Filamentation of unstable vortex structures via separatrix crossing: A quantitative estimate of onset time. *Phys. Fluids,* **A1,** 181–184.

Schouten, M. W., W. P. M. De Ruijter, P. J. Van Leeuwen, and J. R. E. Lutjeharms, 2000: Translation, decay and splitting of Agulhas rings in the southeastern Atlantic Ocean. *J. Geophys. Res.,* **105,** 21 913–21 925.

Simmons, H., and D. Nof, 2000: Islands as eddy splitters. *J. Mar. Res.,* **58,** 919–956.

Smith, D. C., IV, and J. J. O'Brien, 1983: The interaction of a two-layer isolated mesoscale eddy with bottom topography. *J. Phys. Oceanogr.,* **13,** 1681–1697.

Smith, L. T., 1992: Numerical simulations of stratified rotating flow over finite amplitude topography. *J. Phys. Oceanogr.,* **22,** 686–696.

Sutyrin, G. G., and G. R. Flierl, 1994: Intense vortex motion on the beta plane: Development of the beta gyres. *J. Atmos. Sci.,* **51,** 773–790.

——, and Y. Morel, 1997: Intense vortex motion in a stratified fluid on the beta-plane: An analytical theory and its validation. *J. Fluid Mech.,* **336,** 203–220.

Thierry, V., and Y. Morel, 1999: Influence of a strong bottom slope on the evolution of a surface-intensified vortex. *J. Phys. Oceanogr.,* **28,** 911–924.

Van Geffen, J. H. G. M., and P. A. Davies, 2000: A monopolar vortex encounters an isolated topographic feature on a β-plane. *Dyn. Atmos. Oceans,* **32,** 1–26.

Verron, J., and C. Le Provost, 1985: A numerical study of quasi-geostrophic flow over topography. *J. Fluid Mech.,* **154,** 231–252.

Wang, G., and W. Dewar, 2003: Meddy–seamount interactions: Implication for the Mediterranean salt tongue. *J. Phys. Oceanogr.,* in press.

Weiss, J., 1991: The dynamics of enstrophy transfer in two-dimensional hydrodynamics. *Physica D,* **48,** 273–294.